FISEVIER

Contents lists available at ScienceDirect

# **Biomaterials Advances**

journal homepage: www.journals.elsevier.com/materials-science-and-engineering-c





# 3D printing a biocompatible elastomer for modeling muscle regeneration after volumetric muscle loss

Wisarut Kiratitanaporn <sup>a,1</sup>, David B. Berry <sup>b,c,1</sup>, Anusorn Mudla <sup>d</sup>, Trevor Fried <sup>a</sup>, Alison Lao <sup>b</sup>, Claire Yu <sup>b</sup>, Nan Hao <sup>d</sup>, Samuel R. Ward <sup>a,c,e,\*</sup>, Shaochen Chen <sup>a,b,\*\*</sup>

- <sup>a</sup> Department of Bioengineering, University of California, 9500 Gilman Dr. San Diego, La Jolla, CA 92093, USA
- <sup>b</sup> Department of NanoEngineering, University of California, 9500 Gilman Dr. San Diego, La Jolla, CA 92093, USA
- Department of Orthopaedic Surgery, University of California, 9500 Gilman Dr. San Diego, La Jolla, CA 92093, USA
- d Department of Section of Molecular Biology, Division of Biological Sciences, University of California, 9500 Gilman Dr. San Diego, La Jolla, CA, 92093, USA
- <sup>e</sup> Department of Radiology, University of California, 9500 Gilman Dr. San Diego, La Jolla, CA 92093, USA

#### ARTICLE INFO

Keywords:
3D printing
DLP
Poly glycerol sebacate acrylate
Volumetric muscle loss
Skeletal muscle

#### ABSTRACT

Volumetric muscle loss (VML) injuries due to trauma, tumor ablation, or other degenerative muscle diseases are debilitating and currently have limited options for self-repair. Advancements in 3D printing allow for the rapid fabrication of biocompatible scaffolds with designer patterns. However, the materials chosen are often stiff or brittle, which is not optimal for muscle tissue engineering. This study utilized a photopolymerizable biocompatible elastomer – poly (glycerol sebacate) acrylate (PGSA) – to develop an *in vitro* model of muscle regeneration and proliferation into an acellular scaffold after VML injury. Mechanical properties of the scaffold were tuned by controlling light intensity during the 3D printing process to match the specific tension of skeletal muscle. The effect of both geometric (channel sizes between 300 and 600 µm) and biologic (decellularized muscle extracellular matrix (dECM)) cues on muscle progenitor cell infiltration, proliferation, organization, and maturation was evaluated *in vitro* using a near-infrared fluorescent protein (iRFP) transfected cell line to assess cells in the 3D scaffold. Larger channel sizes and dECM coating were found to enhance cell proliferation and maturation, while no discernable effect on cell alignment was observed. In addition, a pilot experiment was carried out to evaluate the regenerative capacity of this scaffold *in vivo* after a VML injury. Overall, this platform demonstrates a simple model to study muscle progenitor recruitment and differentiation into acellular scaffolds after VML repair.

#### 1. Introduction

Skeletal muscle is the most abundant tissue in the body and possesses an inherent capacity to regenerate after injury, even in skeletally mature individuals [1]. However, this regenerative response fails with volumetric loss (VML) injuries, defined as the loss of 15 % or more of the total muscle mass [2,3]. VML injuries occur as a result from traumatic or surgical removal of a large volume of muscle and can occur in both military and civilian populations [4,5]. The size of a VML injury impedes normal muscle regeneration, and often resolves in fibrous scar formation, resulting in chronic functional deficits and diminished force

#### production [6].

The current gold standard for treating a VML injury is autologous muscle flap transfer, which is associated with donor site morbidity and generally has poor outcomes, with nearly 10 % of these procedures resulting in complete graft failure [2]. Furthermore, in patients with extensive injury, where the availability of donor tissue is limited, there may not be enough healthy tissue to use as a donor. To combat the limitations of autologous muscle flap transfer and provide clinical alternatives to VML treatment, several tissue-engineered constructs (both cellular and acellular) have been developed as off-the-shelf alternatives [7–25]. The general goal of these approaches is to induce organized

<sup>\*</sup> Correspondence to: S.R. Ward, 9500 Gilman Drive, MC 0863, La Jolla, CA 92093, USA.

<sup>\*\*</sup> Correspondence to: S. Chen, 9500 Gilman Drive, Structural Materials Engineering Building, Room 245B, La Jolla, CA 92093, USA.

\*\*E-mail addresses: wkiratit@eng.ucsd.edu (W. Kiratitanaporn), dbberry@ucsd.edu (D.B. Berry), amudla@ucsd.edu (A. Mudla), tfried@ucsd.edu (T. Fried), a5lao@ucsd.edu (A. Lao), hyy039@eng.ucsd.edu (C. Yu), nhao@ucsd.edu (N. Hao), s1ward@health.ucsd.edu, s1ward@health.ucsd.edu (S.R. Ward), chen168@eng.ucsd.edu (S. Chen).

<sup>&</sup>lt;sup>1</sup> These authors contributed equally to this work.

muscle regeneration through either the recruitment of the endogenous stem cell population or through direct implantation of muscle progenitor cells into the damaged region. Many groups have employed various fabrication techniques such as decellularization [10,12,17,19], electrospinning [14,26–29], extrusion-based 3D printing [20,30], freeze drying [31], mold casting [7,9], and thermal drawing [16], cell types such as C2C12s [26,31–35], human-derived iPSCs [30], and primary myoblasts [30], and biomolecules such as agrin [26], hepatocyte growth factor [32], and vascular endothelial growth factor [25], demonstrating fair to excellent capacity to regenerate organized skeletal muscle and restore force production. Many of the more successful approaches have employed cell-based regenerative techniques. However, translation to a potential clinical therapy presents a problem; while biomaterials are likely to obtain approval from the Food and Drug Administration (FDA), obtaining approval for the use of allogenic or xenogenic tissue sources – which are more readily obtained than autologous cell sources - is

Due to the FDA regulatory hurdles and immunogenic concerns associated with cellular tissue-engineered scaffolds, acellular scaffolds are an attractive candidate for biomedical application in the treatment of VML. Currently, the gold standard for tissue-engineered VML repair is decellularized extracellular matrix (dECM) sheets [37]. These acellular biologic scaffolds are attractive as they contain vital biologic factors thought to be involved in the recruitment of progenitor cells, regulation of macrophage polarization, and tissue regeneration [38]. These scaffolds aim to provide a mechanical and biochemical environment in which local progenitor cells will infiltrate, orient, and differentiate into functional skeletal muscle. However, these mechanisms are not well understood, as no standardized in vitro model of VML currently exists. Histologic examination of dECM scaffolds after prolonged in vivo implantation demonstrated some muscle infiltration and regeneration [37]. Although the muscle that is formed is often not aligned with the native muscle orientation, which is associated with the lack of organization of dECM sheet scaffolds. Another solution is naturally derived hydrogels, which have been extensively utilized in the tissue engineering community due to their favorable biocompatibility, biodegradability, bioactivity, and ability to be fabricated into precise geometric structures [39,40]. However, they possess low mechanical stiffness and undergo swelling in aqueous environments, thus limiting their use in skeletal muscle tissue engineering applications [41]. These factors have driven interest towards utilizing synthetic biomaterials due to their low batch-to-batch variability and high level of tunability and control in terms of mechanical properties and functionalization for tissue engineering applications [42].

Poly (glycerol sebacate) (PGS) is a highly tunable, biodegradable elastomer originally developed by Wang et al. [43]. PGS is highly elastic, has robust mechanical properties, and is able to maintain its structural integrity in an aqueous environment due to its low swelling ratio, making it a natural candidate for skeletal muscle tissue engineering applications [43,44]. However, due to its high viscosity and glass transition temperature, it has traditionally been difficult to fabricate PGS with microscopic geometric alignment, which is a crucial feature for skeletal muscle organization and function. Recently, Wang et al. [45] has demonstrated a method (originally developed by Nijst et al. [46]) to modify PGS with photocrosslinkable acrylate groups to make poly (glycerol sebacate) acrylate (PGSA), to facilitate the fabrication of structures using digital light projection (DLP) based 3D printing. This allowed for the precise fabrication of structures with tunable material properties similar to those of skeletal muscle and the ability to print micro-scale geometric features, which can guide tissue organization. While PGSA has many favorable properties for musculoskeletal tissue engineering, historically it has not been widely used as it is difficult to manufacture them into functional devices.

DLP-based 3D printing technology is an emerging 3D printing technology that allows for rapid fabrication of complex scaffolds with intricate architecture and micron scale resolution from

photopolymerizable polymers within seconds [47,48]. However, many of the materials compatible with this printing method are either too brittle or too soft to withstand the dynamic forces of muscle *in vivo* (specific tension: 107 kPa–225 kPa [49–52]; up to 40 % strain [53]). To address challenges in fabricating scaffolds for VML repair, we propose to utilize PGSA to fabricate a scaffold capable of recapitulating the mechanical and microstructural environment of skeletal muscle using a novel 3D printing technique in conjunction with a dECM coating to promote muscle infiltration and proliferation.

The primary goal of this study is to investigate the in-vitro cellular response of muscle progenitor cells in PGSA scaffolds with anisotropically aligned microchannels of varying physiologically informed sizes. We will evaluate how muscle progenitor cells respond to durotaxic environmental cues by tuning the mechanical properties of PGSA to that of the specific tension of skeletal muscle and topotactic environmental cues by changing the geometry (size) of hollow channels. Furthermore, we will evaluate the effect of haptotactic environmental cues by incorporating a muscle decellularized extracellular matrix (dECM) coating. In this study, we will promote cellular infiltration into an acellular scaffold for VML treatment by seeding muscle progenitor cells around acellular PGSA scaffolds and allow the cells to migrate into and proliferate in the microchannels naturally over time without encapsulating or seeding them directly into the construct in order to mimic endogenous cellular response following implantation of acellular scaffold into a VML injury site. Key outcome measures of muscle alignment, proliferation, and differentiation are assessed to explore the potential of PGSA microchannel scaffold in guiding myoblast assembly and formation of skeletal muscle fibers for VML tissue engineering applications. We hypothesize that a dECM coated PGSA scaffold would provide a geometric, mechanical, and biochemical environment for muscle progenitor cells to infiltrate, proliferate, and mature in vitro. The secondary goal of this study is to perform a preliminary investigation to evaluate the regenerative capacity of 3D printed PGSA scaffolds in an animal model of VML. Overall, this work demonstrated a novel approach for fabricating and evaluating acellular scaffolds for VML repair.

# 2. Materials and methods

# 2.1. Materials

Sebacic acid, glycerol, and ethyl acetate were purchased from Fisher Scientific (Waltham, MA). Anhydrous dichloromethane (DCM), triethylamine (TEA), 4-dimethylaminopyridine (DMAP), diphenyl(2,4,6-trimethylbenzoyl)phosphine oxide (TPO), acryloyl chloride, and chloroform-d (CDCl $_3$ ) were purchased from MilliporeSigma (St. Louis, MO). For cell culture, Dulbecco's Modified Eagle Medium (DMEM), fetal bovine serum (FBS), penicillin/streptomycin (P/S), and Normocin<sup>TM</sup> were purchased from Thermo Fisher Scientific (Waltham, MA).

#### 2.2. PGS synthesis

The synthesis of PGS was similar to a previously published protocol reported with minor modifications (Supplementary Fig. 1A) [43]. Briefly, glycerol and sebacic acid were mixed at an equimolar ratio under argon gas and constant stirring at 140  $^{\circ}$ C for 1 h in a round bottom flask. Once sebacic acid and glycerol were evenly mixed and melted, the polycondensation polymerization reaction was carried out by reducing the temperature to 120  $^{\circ}$ C and the pressure to 35 Pa. The polycondensation reaction was carried out for the next 15 h with the pressure maintained at 35 Pa.

# 2.3. PGSA synthesis

The acrylation of PGS to create PGSA followed a previously published protocol [46]. Briefly, 30 g of PGS was dissolved in 300 ml of DCM at room temperature under constant stirring for 1 h followed by the

addition of 30 mg of DMAP under argon gas. The temperature was then reduced to 0 °C in an ice bath for 10 min. Then, 7 ml of TEA was added dropwise into the reaction flask followed by the dropwise addition of 3.3 ml of acryloyl chloride. The acrylation reaction was continued for the next 24 h under room temperature without any exposure to light. DCM was then removed from the solution by rotary evaporation at 40 °C. Excess ethyl acetate was then added to the remaining solution to precipitate the TEA out. The PGSA prepolymer solution was then filtered repeatedly, subjected to rotary evaporation at 45 °C and 5 Pa to remove excess ethyl acetate, and stored at -20 °C in the dark until use. One batch of PGSA was synthesized and used for all the experiments that were carried out.

# 2.4. <sup>1</sup>H NMR characterization

 $^{1}$ H nuclear magnetic resonance ( $^{1}$ H NMR) spectra of PGS and PGSA were collected at 298 K using a 600 MHz Bruker Avance III spectrometer fitted with a 5 mm broadband inverse detection probe with z-axis gradients using CDCl $_{3}$  as the solvent to confirm the chemical identity and structure of the final synthesized products. The spectra were analyzed with Bruker TopSpin software.

# 2.5. PGSA-based printing solution preparation

The PGSA printing solutions were prepared by mixing the PGSA prepolymer with 4 % (w/v%) TPO and 0.01 % (w/v%) tartrazine (MilliporeSigma, St. Louis, MO) prior to printing.

# 2.6. DLP-based 3D printing of PGSA

The PGSA scaffolds were fabricated using an in-house developed DLP-based 3D printing system, called microscale continuous optical bioprinting (µCOB) [54]. The DLP printing system consists of a 385 nm light source, a digital micromirror device (DMD) chip (Texas Instruments, Dallas, TX) for optical pattern manipulation, a series of optical projection lens, a computer running an in-house developed 3D printing software for hardware synchronization and digital uploading of photomasks to the DMD chip, a static stage for holding the prepolymer resin reservoir, and a motion-controlled probe with methacrylated coverslip bonded to it that continuously moves up in the z-direction to enable continuous printing of 3D scaffolds (Fig. 1A). The digital patterns of the scaffolds were designed using a MATLAB script and uploaded into the custom 3D printing software as BMP files. 3D reconstructions of the scaffolds can be found in Supplementary Figs. 2, 3. .STL files of the scaffolds are additionally provided as supplementary information.

First, the 385 nm light was projected from the light source onto the DMD chip as the digital patterns were sequentially uploaded into the DMD chip from the computer through the 3D printing software. The optical projection lens then guided the optically generated patterns from the DMD chip into a polydimethylsiloxane (PDMS) coated reservoir containing PGSA prepolymer bioink. The motion-controlled probe slowly moved up in the z-direction at a speed of 0.034 mm/s during the printing process as the PGSA construct was being photopolymerized to allow for continuous layer-by-layer printing of the scaffolds on the focal plane. The DMD device that was used in this printing system consists of

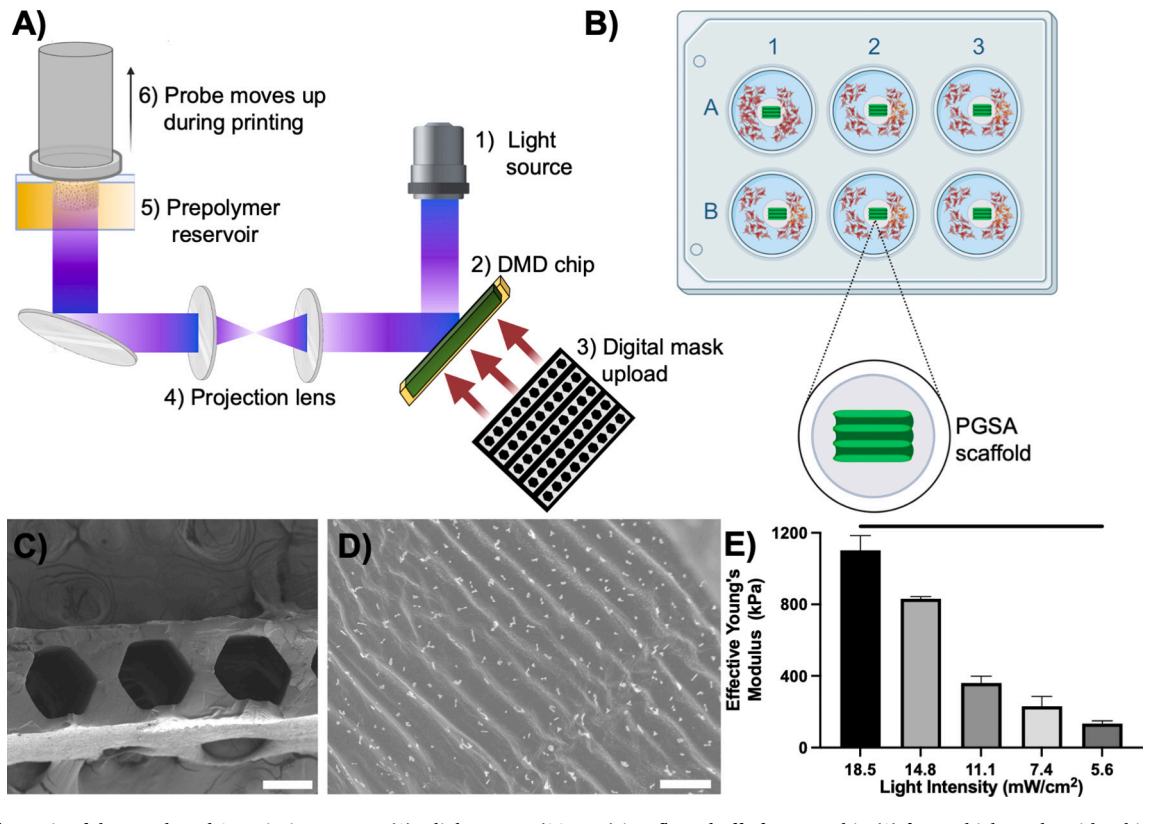


**Fig. 1.** A.) Schematic of the DLP-based 3D printing system. (1) a light source (385 nm) is reflected off of a DMD chip (2) from which masks with arbitrarily complex geometry (3) are continuously uploaded. The reflected light from the DMD chip goes through a series of projection lenses (4) into a prepolymer reservoir (5) containing PGSA. The pattern of light reflected into the prepolymer reservoir crosslinks PGSA and sticks to a moving probe (6) allowing for continuous smooth structures to be fabricated. B) Schematic outlining the cell seeding strategy to replicate muscle progenitor cell infiltration into a PGSA scaffold after VML injury. C) SEM of a PGSA scaffold with 450 μm diameter channels (*Scale bar* =  $200 \, \mu m$ ). D) SEM of a sectioned PGSA scaffold coated with dECM (small specular objects), demonstrating the longitudinal microgrooves that are formed during the continuous 3D printing process (*Scale bar* =  $10 \, \mu m$ ). E) Effective Young's modulus of PGSA as a function of the light exposure intensity. A light exposure of 5.6 mW cm<sup>-2</sup> was used in this study, which simultaneously allowed for stiffness similar to that normal skeletal muscle (107 kPa–225 kPa) [49–52] as well as the ability to print fine structures without overpolymerization. Sidak *post hoc* tests identified significant differences between each light exposure intensity (bar, p < 0.0175).

individual micromirrors with a size of  $7.56~\mu m$ . Using focusing optics, we were able to achieve a printing resolution as small as 3  $\mu m$ . Once printed, PGSA scaffolds were then rinsed in isopropyl alcohol (IPA), DI water, and PBS.

To assess if modulating the biochemical environment of PGSA scaffolds improved cell orientation, proliferation, or maturation, half of the scaffolds were coated in porcine skeletal muscle dECM. Under sterile conditions, 400  $\mu$ l of 6 mg ml $^{-1}$  dECM in PBS [55] was placed into each well of a 24 well plate, each containing a single scaffold. Plates were placed on a low-speed shaker for 48 h in order to facilitate dECM infiltration into the microchannels. Then, plates were placed in an incubator and the PBS was allowed to evaporate. dECM deposition was verified using SEM (Fig. 1D). Scaffolds were sterilized under UV light for 30 min prior to cell seeding.

#### 2.7. Nanoindentation

PGSA rectangular specimens (5 mm  $\times$  5 mm) printed at varying light exposure intensities were tested using a Piuma nanoindenter (Optics11, Amsterdam, Netherlands) to measure the effective Young's modulus. The total time it took to 3D print the whole scaffold was 60s. The samples were mounted on the bottom of a petri dish and submerged in phosphate buffer saline (PBS) solution at room temperature during testing with the nanoindenter tip remaining well below the meniscus of the PBS solution. A spherical probe with the tip radius of 48.5  $\mu$ m and a cantilever stiffness of k = 4.24 N m<sup>-1</sup> was used. Nanoindentation data was analyzed based on the Hertz contact model [56] with a Poisson's ratio of 0.5 [57,58]. For each sample, indentations were carried out in triplicate and the average was calculated. For each experimental condition, 5–6 individual samples (n=5–6) were tested.

# 2.8. Nuclear marker cell line construction

The donor plasmid was generated using Gibson assembly method. Briefly, H2B-iRFP fragment was PCR amplified from a H2B-iRFP plasmid [59] and cloned into pLenti-puro vector (Addgene 39,481; Fig. 2B). Gibson reaction was performed according to the manufacturer's protocol (NEB E5520S). The reaction mixture was transformed into *E. coli* and the correct clone were selected and sequenced. The donor plasmid

sequence can be provided upon reasonable request.

HEK293T were ordered from ATCC (ATCC CRL-11268) and regularly tested negative for Mycoplasma using Mycoplasma detection kit (Southern Biotech). HEK293T cells were cultured in Dullbecco minimal essential medium (DMEM: Thermo Scientific HyClone #SH30022FS) supplemented with 10 % fetal bovine serum, 4 mM L-glutamine, 100 I.U.  $ml^{-1}$  penicillin and 100 µg  $ml^{-1}$  streptomycin at 37 °C, 5 % CO<sub>2</sub> and 90 % humidity. Lentivirus was generated by transfecting HEK 293 T with 9  $\mu g$  of the donor plasmid, 6  $\mu g$  of psPAX2 (Addgene 12260) and 3  $\mu g$  of pMD2.G (Addgene 12259) using 36  $\mu$ l of Fugene HD (Promega E2311) in a 10 cm dish. The supernatant was collected 24 h after the transfection and filtered through 0.45 µm filter. Polybrene (Sigma-Aldrich 107689) was added to the supernatant to the final concentration of  $8\mu g \text{ ml}^{-1}$ . The supernatant was added to C2C12 cells, previously seeded at 300,000 cells per well in a 6-well plate. The cells were screened with 1  $\mu g$  ml<sup>-1</sup> puromycin for 48 h. The surviving cells were cultured until confluent and passaged to a 10 cm dish. Single iRFP positive cells were FACS sorted into a 96-well plate and cultured until a colony was visibly formed. Homogeneity was confirmed by observing the cells under fluorescent microscope. The final clone was checked for the presence of the pCMV-NLS-iRFP with PCR.

# 2.9. Cell culture and seeding

C2C12 cells (ATCC, Manassas, VA) were expanded in growth medium containing high-glucose DMEM, 10 % FBS, 1 % P/S, and 0.2 % Normocin. C2C12 cells at passage 1 were used for iRFP nuclear marker cell line construction. iRFP-transfected C2C12s were used for subsequent experiments at passage 6. Prior to cell seeding, 3D printed PGSA scaffolds were primed in high-glucose DMEM for 30 min at 37 °C in an incubator. Then, the scaffolds were transferred to a 24-well glass bottom cell culture plates (Cellvis, Mountain View, CA) for cell seeding. C2C12 cells were seeded as a 10  $\mu$ l droplet on both ends of each PGSA scaffold for a total seeding density of 250,000 cells per scaffold (Fig. 1B). The scaffolds were then incubated at 37 °C for 2 h with the addition of 15  $\mu$ l of growth media (DMEM, 10 % FBS, 1 % P/S, 0.2 % Normocin<sup>TM</sup>) to each well at every 30-minute interval. After 2-hour incubation, the scaffolds and seeded cells were checked under the light microscope to ensure cell attachment on both ends of each scaffold. Subsequently, 500  $\mu$ l of

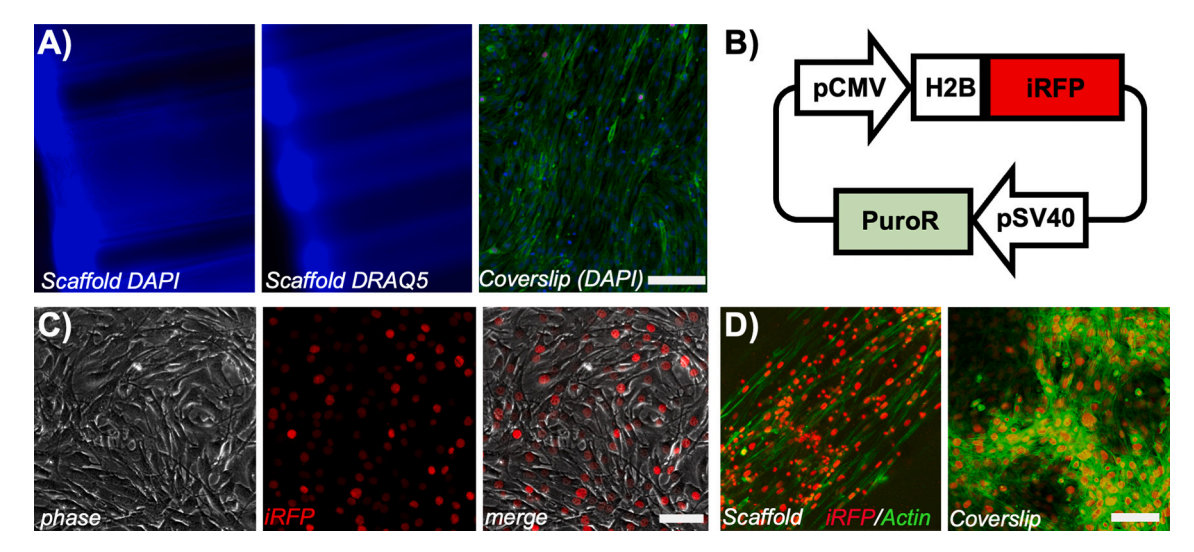


Fig. 2. Creating a transfected cell line to assess nuclear staining of cells in a PGSA scaffold. A) PGSA's autofluorescence in the DAPI channel along with the material's physical adsorption of far-red nuclear dye DRAQ5 makes it challenging for visualization of cells within the microchannel construct due to low signal-to-noise ratio. B) A schematic of the lentivirus donor plasmid showing the DNA elements destined to be integrated into the genome of C2C12 cells. The expression of H2B-iRFP is under cytomegalovirus (CMV) promoter while the expression of puromycin resistant gene is under SV40 promoter. C) Phase (left) and immunofluorescent (middle) images of the iRFP nuclear transfected C2C12 cell line used in these experiments. D) iRFP nuclear transfected C2C12 cells in the scaffold (left) and coverslip control (right) demonstrate clear imaging of the nucleus with no fluorescent noise from the scaffold itself. Scale bar = 300  $\mu$ m (A, D). Scale bar = 100  $\mu$ m (C). (For interpretation of the references to colour in this figure legend, the reader is referred to the web version of this article.)

growth medium was added to each well for cell culture. The cells were maintained in growth media for up to 7 days for cell alignment and proliferation analyses and up to 12 days for differentiation analysis.

# 2.10. Immunofluorescence staining of cell markers

For cell alignment and proliferation analyses, at each timepoint the scaffolds were rinsed three times with PBS before fixing in 4 % paraformaldehyde (PFA) solution for 30 min at room temperature on a shaker. Once fixed, the scaffolds were rinsed three times in PBS and blocked and permeabilized for 1 h in a block/perm solution comprising of 5 % (w/v) bovine serum albumin (BSA, GeminiBio) with 0.2 % (w/v) Triton X-100 (MilliporeSigma, St. Louis, MO) in PBS on a shaker. Then, scaffolds were incubated with rabbit polyclonal anti-Ki67 primary antibody (1:100; ab15580, Abcam) diluted in 5 % BSA solution overnight at 4 °C. The scaffolds were then rinsed three times with PBS and incubated with CF555 goat anti-rabbit secondary antibody (H + L) (1:200; Biotium) for 1 h on a shaker followed by three PBS washes. After that, the scaffolds were incubated with CF488A conjugated phalloidin for another 1 h and rinsed three times in PBS. Samples were then imaged with a Leica SP8 confocal microscope.

For cellular differentiation analysis, at each timepoint the scaffolds were rinsed three times with PBS before fixing in 4 % paraformaldehyde (PFA) solution for 30 min at room temperature on a shaker. Once fixed, the scaffolds were rinsed three times in PBS and blocked and permeabilized for 1 h in a block/perm solution comprising of 5 % (w/v) bovine serum albumin (BSA, GeminiBio) with 0.2 % (w/v) Triton X-100 (MilliporeSigma, St. Louis, MO) in PBS on a shaker. Then, scaffolds were incubated with mouse MF20 monoclonal antibody (1:10; Developmental Studies Hybridoma Bank, University of Iowa, Iowa City, IA) diluted in 5 % BSA solution overnight in 4 °C. The scaffolds were then rinsed three times with PBS and incubated with CF555 goat anti-mouse secondary antibody (H + L) (1:200; Biotium) for 1 h on a shaker followed by three PBS washes. After that, the scaffolds were incubated with CF488A conjugated phalloidin for 1 h and rinsed three times in PBS. Samples were imaged with a Leica SP8 confocal microscope.

# 2.11. Gastrocnemius muscle decellularization

Fresh porcine gastrocnemius muscle was freshly isolated from threemonth old Yorkshire pigs that were supplied by S&S Farms (Ramona, CA), an animal vendor approved by the Institutional Animal Care and Use Committee (IACUC) at the University of California San Diego (UCSD). A lethal dose of pentobarbital was administered to the pigs for euthanasia. The gastrocnemius muscles of the sacrificed pigs were immediately harvested and transported to the lab on ice. Excess residual blood was removed through rinsing, and the tissues were cut into 2-3 mm³ pieces and stored in plastic tubs containing PBS supplemented with 1 % ( $\nu/\nu$ ) antibiotic/antimycotic (ABAM) (ThermoFisher Scientific) at  $-80\,^{\circ}$ C until decellularization. To ensure that the harvested tissues were preserved as best as possible in terms of quality and integrity, all the steps leading up to tissue storage were performed within 2 h of harvesting.

All steps in the decellularization process were performed in an incubator shaker running at 120 rpm with the temperature set to 37  $^{\circ}$ C. All solutions were supplemented with 1 % (v/v) ABAM and 0.01 mM phenylmethylsulfonyl fluoride (PMSF, Sigma-Aldrich) except for trypsin-EDTA (Gibco<sup>TM</sup>) and Sorensen's Digest Buffer solution.

First, the tissue was placed into tubs containing hypotonic solution and frozen at  $-80\,^{\circ}\text{C}$ . Then, the tissue was thawed and placed in an incubator shaker for 2 h. Hypotonic solution was then replaced with fresh hypotonic solution, and the freeze-thaw cycle was repeated three times. Once the freeze-thaw cycle was complete, the tissue was rinsed three times in PBS with 30-minute rinses in between and then washed in 0.05 % trypsin-EDTA solution for 1 h. After digestion in trypsin-EDTA solution, the tissue was rinsed three times in PBS for 30 min. The

tissue was then washed for 72 h in 2 % Triton X-100 and 0.8 % NH<sub>4</sub>OH solution for 72 h with 2–3 changes of solution per 24 h and rinsed three times in PBS for 30 min. Then, the tissue was washed in 100 % isopropanol for 2 h before being rinsed three times in PBS for 30 min. Next, the tissue was incubated in 0.5 % (w/v) sodium dodecyl sulfate (SDS) (Sigma-Aldrich) solution in PBS for 4 h followed by three 30-minute washes in PBS and rinsed in Sorensen's buffer digest solution for another 30 min. The tissue was then digested in Sorensen's buffer digest solution containing DNase (Sigma-Aldrich) for 24 h. Finally, the tissue was rinsed for 24 h in MilliQ water and stored in 70 % ethanol in 4 °C.

# 2.12. Quantification of dsDNA content

Decellularized muscle tissue along with its native muscle tissue control were frozen at  $-80~^{\circ}\text{C}$  and lyophilized for 48 h. Next, 50 mg of lyophilized muscle dECM as well as its respective lyophilized native tissue control were digested in papain solution (Sigma-Aldrich) containing 0.1 mg ml $^{-1}$  papain in 0.2 M sodium phosphate buffer solution for 20 h at 65  $^{\circ}\text{C}$  on an incubator shaker. Once digestion was complete, the supernatant was collected following a 10 min centrifugation at 10,000 rpm. To measure the dsDNA content, the Quant-iTTM Pico-GreenTM dsDNA assay kit was used following the manufacturer's instructions. The dsDNA content of the decellularized muscle was found to be 39.43 ng mg $^{-1}$   $\pm$  0.56, below the required 50 mg mg $^{-1}$  dsDNA limit.

# 2.13. Preparation of gastrocnemius muscle dECM coating

First, the dECM tissue was washed in 70 % ethanol for 24 h on a shaker followed by 24 h wash in sterile MilliQ water before being frozen and lyophilized for 48 h. The lyophilized muscle dECM was then placed into a cryomilling chamber containing three 10 mm stainless steel milling balls. This setup was then subjected to cooling in liquid nitrogen for 3 min. Once cooled, the muscle dECM was cryomilled for 2 min at 30 Hz using the Retstch<sup>TM</sup> MM400 mixer mill (Verder Scientific, Newtown, PA). Milled muscle dECM powder was then digested in pepsin digest solution containing 1 mg ml $^{-1}$  pepsin (Sigma-Aldrich) in 0.1 M HCl for 24 h on a shaker at room temperature. The pepsin solubilized solution was then neutralized by NaOH addition and frozen in  $-80\,^{\circ}\text{C}$  overnight before being lyophilized for 48 h. Once lyophilized, the lyophilized muscle dECM was cryomilled again under the same conditions as previously mentioned and stored at room temperature until use.

# 2.14. In vitro image analysis

All images were assessed using a custom written Matlab script (Mathworks, Natick, MA). Images were imported as .tif files and the channels were identified using the roipoly tool. To assess cellular orientation and proliferation, three samples per experimental condition (n=3) were examined. Images were rotated to align the channels to  $0^{\circ}$ , and actin alignment was assessed by calculating a local orientation map of image using a rotating line segment as a structuring element for a morphological opening. Nuclei were identified and binarized using the adaptthresh function. The percentage of Ki67+ nuclei was calculated as the number of cells that were positive for both Ki67 and H2B-iRFP. In cases where adjacent nuclei were overlapping, a watershed transform was used to segment the nuclei. For cell fusion studies, six to twelve samples per experimental condition (n = 6-12) were examined and the percentage of MHC+ area was calculated as the area of cells that stain positive for MHC divided by the area of cells that stained positive for actin.

# 2.15. In vivo evaluation of the 3D printed PGSA scaffold

Four female Lewis rats were used for this study. All protocols were approved by the University of California, San Diego Institutional Animal Care and Use Committee (Protocol #S09030), and all animals were

approximately 4 months of age at the start of the study. 3D printed PGSA scaffolds were prepared for this pilot study (3 mm  $\times$  3 mm  $\times$  5 mm; Fig. 6A). All scaffolds had 450  $\mu m$  diameter channels running the length of the scaffold, and two of the four scaffolds were treated with a dECM coating (see Section 2.6). Under anesthesia, a defect approximately 4 mm  $\times$  4 mm  $\times$  7 mm was manually resected in the tibialis anterior using a scalpel (Fig. 6B). The scaffold was placed in the defect aligned longitudinally with the muscle fibers. The fascia was sutured to keep the scaffold in place, and the skin was stapled closed. All rats were returned to cages and supplied with ad libitum food and water until they were sacrificed at 28 days post-operation. The tibialis anterior was immediately harvested and snap frozen for histologic analysis.

#### 2.16. Histologic analysis

For preliminary evaluation of a 3D printed PGSA scaffold for VML regeneration, 8 µm thick axial sections of the scaffolds were made using a cryostat. Sections evaluated in this study were from the center of the scaffold, 2.5 mm from either border. Sections were stained with Haemotoxylin and Eosin to visualize gross scaffold and tissue composition. Masson's trichrome stain was also performed to visualize the connective tissue and muscle tissue outside of and inside of the scaffold.

# 2.17. Statistical analysis

Prism 9 (Graphpad, La Jolla, CA) was used to perform all statistical analysis. Normality of samples was checked with the Shapiro-Wilk test to ensure parametric statistics were appropriate. For mechanical properties analysis, a one-way Analysis of Variance (ANOVA) with *post hoc* Sidak tests was performed to determine the effect of light intensity on Youngs Modulus. For cell proliferation (%KI67+) and cell fusion (%MHC+) analysis, separate two-way ANOVAs with *post hoc* Sidak tests were performed to determine the effect of channel size and dECM content at each time point. Threshold for significance ( $\alpha$ ) was set to 0.05 for all analyses. All data are reported as mean +/- standard deviation.

#### 3. Results

# 3.1. PGSA synthesis

The synthesis of PGSA followed a two-step chemical synthesis scheme (Supplementary Fig. 1A). First, the PGS prepolymers were synthesized through a polycondensation reaction between glycerol and sebacic acid for 15 h followed by the acrylation of the hydroxyl groups on the PGS backbone by reacting it with acryloyl chloride to obtain PGSA. The successful synthesis of PGS and PGSA prepolymers were confirmed by  $^1\mathrm{H}$  NMR analysis (Supplementary Fig. 1B). In addition,  $^1\mathrm{H}$  NMR also confirmed successful acrylation of the PGS backbone by the presence of the chemical shifts at  $\delta=6.5,\,6.1,\,\mathrm{and}\,5.9$  ppm, indicating the presence of acrylate groups. Our synthesized PGSA yielded a degree of acrylation of 57 %, calculated by taking the average integral of acrylate groups (6.5, 6.1, and 5.9 ppm) divided by the integral of the methylene groups of the sebacate component of the PGS backbone with chemical shift at  $\delta=2.3$  ppm. Only one batch of PGSA was synthesized and used for all the following experiments.

# 3.2. 3D printing of in-vitro PGSA microchannel scaffolds

PGSA scaffolds containing multiple hexagonal microchannel sizes were fabricated in a continuous layer-by-layer manner using an in-house developed DLP-based 3D bioprinter with an LED 385 nm light source (Fig. 1A). Using our DLP-based 3D printing platform, we were able to readily fabricate 3D PGSA scaffolds measuring 2 mm in length and 5 mm in width with various microchannel sizes of 300  $\mu m$ , 450  $\mu m$ , or 600  $\mu m$ . Channel sizes were verified across the long diameter of the hexagonal channel through brightfield Leica imaging and subsequently through

SEM imaging. The microchannel sizes were chosen to replicate the tight packing organization of muscle fascicles, a key microstructural feature of skeletal muscle consisting of multiple bundled myofibers. It took  $<\!4$  min to print each scaffold. The successful fabrication of 3D printed PGSA scaffolds with microchannels possessing fine microstructures was confirmed through SEM imaging (Fig. 1C, D). Longitudinal 10-20  $\mu m$  microgrooves within the channel were observed due to the pixilation effect from the DMD chip during the continuous printing process.

# 3.3. Modulation of PGSA mechanical properties through DLP-based 3D printing

To investigate the ability to control PGSA's mechanical properties through light-based 3D printing, PGSA mechanical testing specimens were printed at light intensities between 5.6 mW cm $^{-2}$  and 18.5 mW cm $^{-2}$ . The Young's modulus of PGSA samples printed at 18.5 mW cm $^{-2}$ , 14.8 mW cm $^{-2}$ , 11.1 mW cm $^{-2}$ , 7.4 mW cm $^{-2}$ , and 5.6 mW cm $^{-2}$  light intensities was 1102  $\pm$  82.4 kPa, 831.8  $\pm$  11.7 kPa, 360.1  $\pm$  38.2 kPa, 230.7  $\pm$  54.6 kPa, and 134.5 kPa  $\pm$  14.6 kPa respectively (Fig. 1E). A significant effect of light intensity on PGSA's stiffness was observed (p < 0.0001) and *post hoc* tests revealed significant differences between all exposure intensities (p < 0.0175). These results confirmed that the mechanical stiffness of PGSA can be precisely controlled to be similar to the specific tension (*i.e.* the maximum force produced per cross sectional area) of skeletal muscle (107 kPa–225 kPa) by varying the light intensity [49–52].

# 3.4. Development of in-vitro VML model using acellular PGSA scaffold and iRFP-C2C12 cell line

To mimic cellular infiltration into acellular PGSA scaffolds with anisotropically aligned microchannels for VML repair, an in-vitro model was developed where C2C12 muscle progenitor cells were seeded around the scaffold to allow for natural cellular infiltration into the microchannels (Fig. 1B). However, PGS-based polymeric scaffolds autofluoresce in blue [57] and in addition to their opacity, it is difficult to distinguish fluorescent signals emitted from the cell nuclei within the scaffold itself using a DAPI stain (Fig. 2A). Several approaches including using nuclear staining dyes with an excitation wavelength outside the spectrum of PGS autofluorescence (i.e. DRAQ5; Fig. 2A) did not improve the image contrast. Far-red nuclear dyes were found to adsorb onto PGSA in addition to staining the nuclei of the cells within the microchannel structure. To circumvent these limitations and preserve the scaffold's structural integrity and spatial distribution of cells, an isogenic cell line of iRFP-C2C12 cells was developed through lentiviral transfection (Fig. 2B, C). By using iRFP-C2C12s for in-vitro modeling of VML treatment using acellular PGSA scaffolds, clear visualization of cell nuclei within the microchannels of the 3D PGSA scaffold was achieved without the presence of background noise from PGS autofluorescence (Figs. 2D; 3).

3D reconstructed confocal images of iRFP-C2C12s taken at various viewing angles within an intact 3D printed PGSA scaffolds demonstrate the orientation of cells within the 3D printed scaffold in high resolution without background noise initially found from PGS autofluorescence (Fig. 3A-C).

# 3.5. Muscle progenitor cell infiltration, proliferation, and maturation in PGSA scaffolds in-vitro

To assess the effect of dECM and channel size on cell proliferation, cells were allowed to migrate into the channels and were assessed at days 1, 3, and 7 after initial seeding (Fig. 4A-F). A significant effect of dECM was found at all timepoints (Day 1: p = 0.0414, Day 3: p < 0.0001, Day 7: p = 0.0135) with overall higher cell proliferation in the dECM containing scaffolds (Fig. 4G-I). A significant effect of channel size was only found at Day 1 (p = 0.0002), driven by low cell proliferation in the

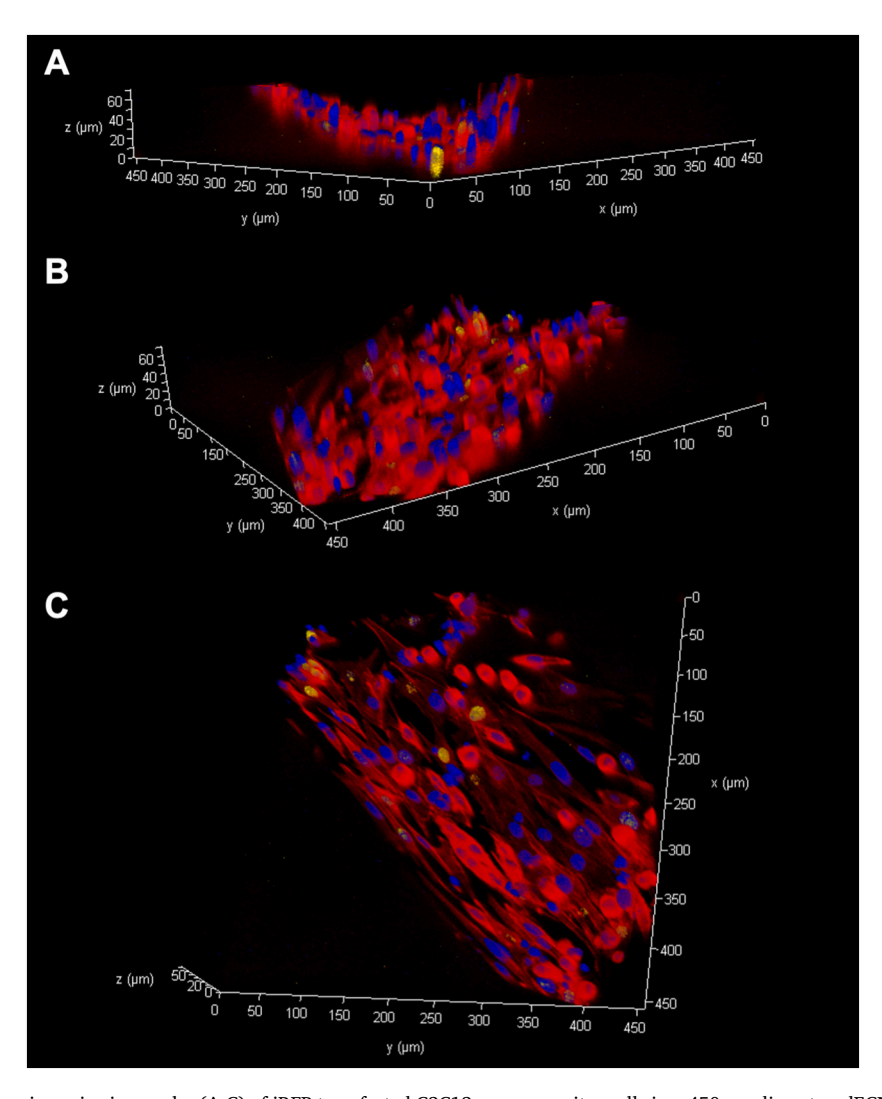


Fig. 3. 3D reconstructions at various viewing angles (A-C) of iRFP transfected C2C12 myoprogenitor cells in a 450 μm diameter, dECM coated PGSA scaffold 3 days after seeding. Actin-red, KI67-yellow, nuclei-blue. (For interpretation of the references to colour in this figure legend, the reader is referred to the web version of this article.)

 $300~\mu m$  channel. Overall, sustained proliferation was observed in the dECM coated scaffolds compared to the non dECM coated scaffolds. However unexpectedly, there was no observed proliferation in the  $300~\mu m$  channels at day 1 (dECM coated) and days 3 and 7 (non DECM coated).

In vivo, skeletal muscle cells are organized into long thin structures, surrounded by extracellular matrix. Multiple cells are often bundled together into larger structures called fascicles. A key requirement for an effective scaffold for cellular organization is the orientation and bundling of infiltrating cells. In general, infiltrating muscle progenitor cells were organized along the same orientation as the channels (Fig. 4 J-L). At day 1, cells in the 300  $\mu m$  and 450  $\mu m$  channels were more aligned with the channel orientation than those in the 600 µm channel indicated by an increase in the frequency of aligned cells close to  $0^{\circ}$ . By day 7 there were no apparent differences between scaffolds with different channel sizes, as the distribution of the frequency of cellular alignment was similar across all channel sizes. Furthermore, the orientation profiles between scaffolds coated with dECM and those without dECM coating was similar, indicating the scaffold coating did not affect cell orientation. Overall, muscle progenitor cells were able to migrate into the channels, proliferate, and align along the channels of the scaffold. Qualitatively, more nuclei were observed in the dECM coated scaffolds (Fig. 4D-F) than the non dECM coated scaffolds (Fig. 4A-C), which may

indicate more cellular infiltration and proliferation.

A key marker of skeletal muscle maturation is the presence of myosin heavy chain. To assess if muscle maturation is influenced by the channel size or dECM content, muscle progenitor cells were allowed to migrate into channels, and proliferate within the scaffolds without the use of induction media (Fig. 5A, B). The area of MHC+ staining normalized by actin+ staining was assessed, as these are 3D constructs and it is difficult to identify individual cells in 3D culture. A significant increase in MHC expression was observed (p < 0.0001) in the dECM coated scaffolds at 12 days after cell seeding (Fig. 5C). Additionally, a significant effect of the channel size (p = 0.0093) was observed, surprisingly driven by slightly decreased MHC expression in the 450  $\mu m$  channels compared to the 300  $\mu m$  and 600  $\mu m$  channels in the dECM coated scaffolds. Qualitative observation of MHC+ fibers revealed more fibrous and elongated MHC+ cells in the dECM coated scaffolds compared to rounded punctate cells in the non dECM coated scaffolds. This suggests that the dECM coating results in a more phenotypic expression of maturing muscle fibers than non dECM coated scaffolds.

# 3.6. In vivo evaluation of a 3D printed PGSA scaffold for VML regeneration

No adverse events were observed in the animal models implanted

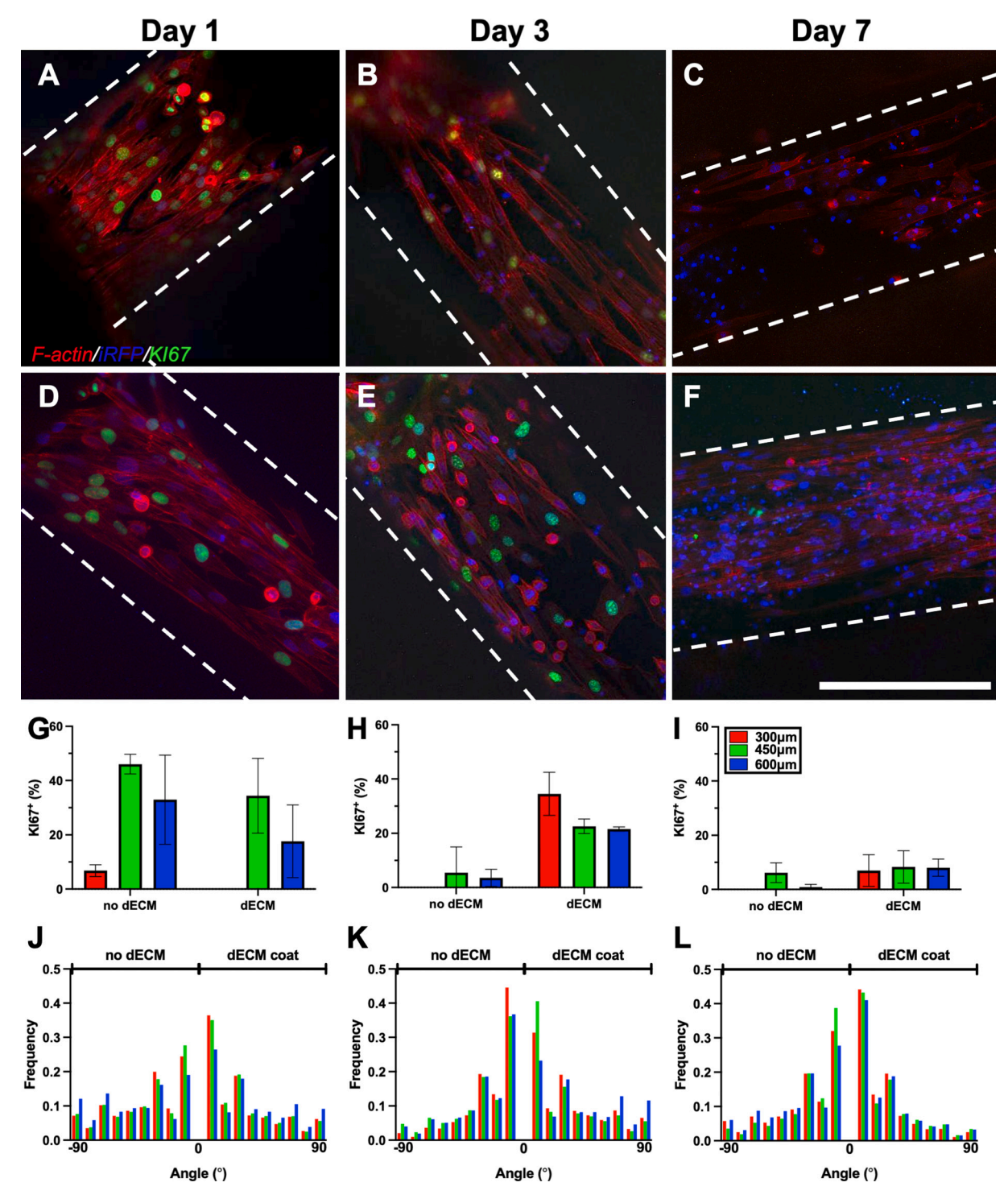


Fig. 4. C2C12 migration, proliferation, and alignment within the PGSA scaffolds. (A-F) confocal images of cells migrating and proliferating (KI67 $^+$ - green) in 450  $\mu$ m diameter channels without dECM coating (A-C) and with dECM coating (D—F) at days 1 (left column), 3 (middle column) and 7 (right column) after seeding. White dashed lines indicate the border of each scaffold. Cell proliferation was measured as %KI67 $^+$  cells at day 1 (G), day 3 (H), and day 7 (I) after seeding. Scaffolds with 300  $\mu$ m (green), and 600  $\mu$ m (blue) diameter channels were assessed with and without dECM coating at all timepoints. Cell alignment (0 $^\circ$  = parallel to channel, 90 $^\circ$  = perpendicular to channel) was assessed at day 1 (J), day 3 (K), and day 7 (L) after seeding. Scale bar = 450  $\mu$ m. n = 3. (For interpretation of the references to colour in this figure legend, the reader is referred to the web version of this article.)

with 3D printed PGSA scaffolds. Gross histologic evaluation indicated a small fibrous ring had formed around the implanted scaffold that was not coated with dECM (Fig. 6C, D), but was not present in the samples that were coated with dECM (Fig. 6E, F). Scaffold structure was still intact after 28 days, and many of the key geometric features of the original scaffold including the size and spacing of aligned microchannels

were present. In both dECM coated and non-dECM coated scaffolds, cellular infiltration deep into the scaffold (2.5 mm) was observed. Generally, a fibrotic ring was observed in the center of each channel, with red stained muscle cells around the periphery. Overall, increased cellular infiltration and new muscle formation was observed in the dECM coated scaffolds (Fig. 6E, F; arrows). These results demonstrate

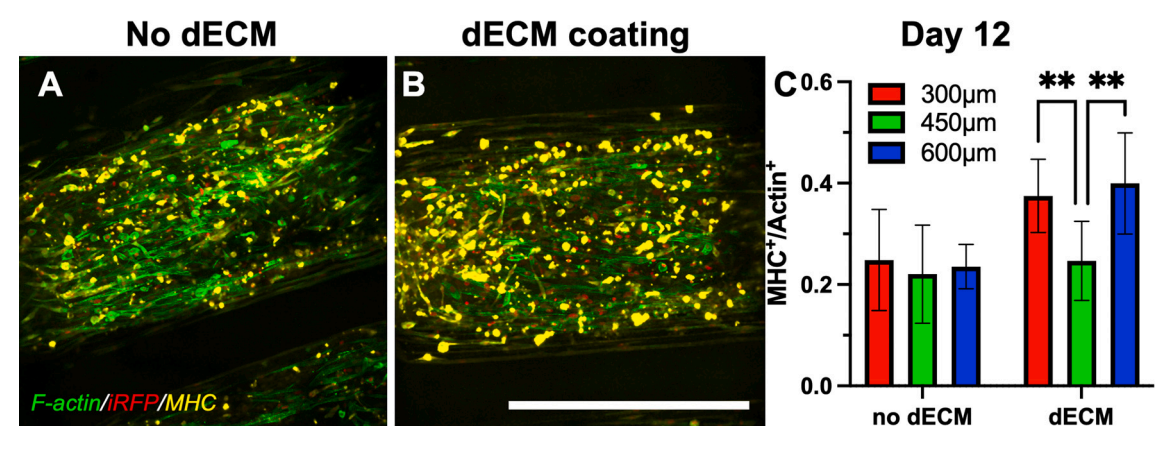
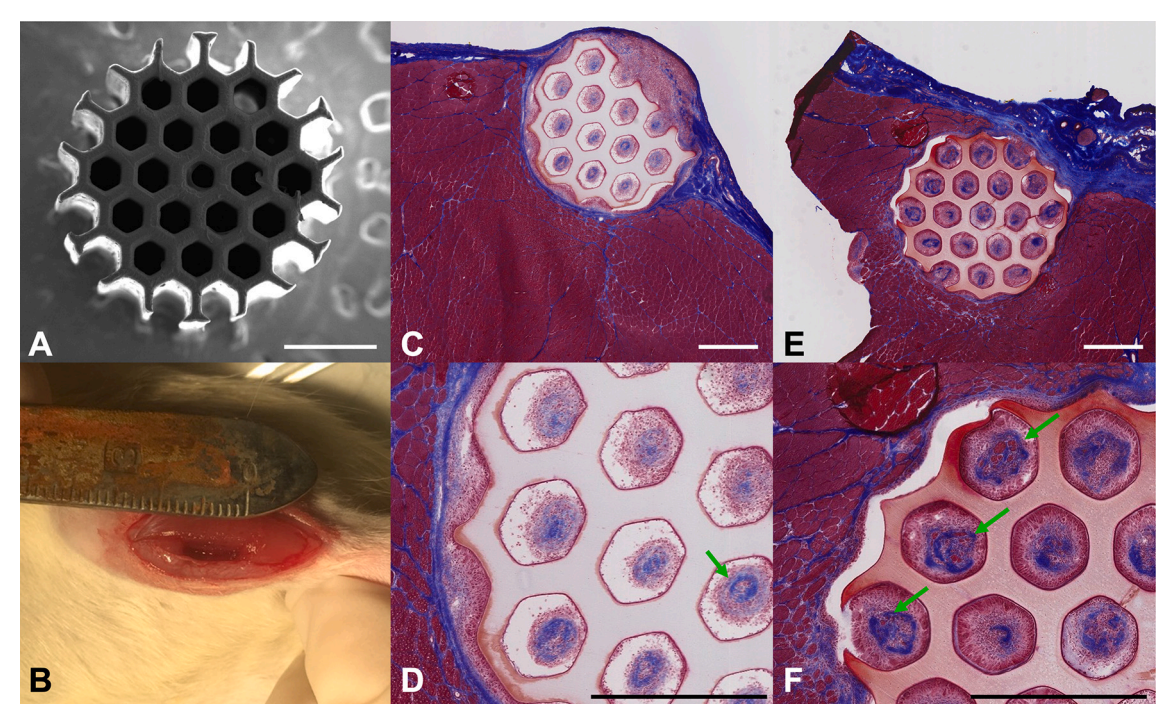


Fig. 5. C2C12 MHC expression at 12 days after seeding in scaffolds without dECM coating (A) and with dECM coating (B) of PGSA scaffolds with 600 μm diameter channel. (C) The area of MHC+ expression normalized by actin+ expression was used to assess myofiber maturation in 3D. \*\* = p < 0.01. Scale bar = 600 μm. n = 6-12.



**Fig. 6.** Preliminary histological assessment of a 3D printed PGSA scaffold to treat a VML injury in a rat. A.) Top down SEM of the implanted scaffold demonstrating the long hollow channels present in the scaffold. B.) Representative image of a volumetric muscle loss injury in a rat. C.) and D.) Representative images of a Masson's Trichrome stained histology of a PGSA scaffold that was not coated with dECM in the middle of the scaffold (2.5 mm from the border). E.) and F.) Representative images of a Masson's Trichrome stained histology of a PGSA scaffold that was coated with dECM in the middle of the scaffold (2.5 mm from the border). Green arrows indicate the presence of muscle fascicle formation deep within the scaffold. Scale bar = 1 mm. (For interpretation of the references to colour in this figure legend, the reader is referred to the web version of this article.)

that muscle can migrate into and form skeletal muscle in 3D printed PGSA scaffolds.

# 4. Discussion

The goal of this study was to develop a PGSA-based scaffold with anisotropically aligned microchannels to investigate the response of muscle progenitor cells in an *in vitro* model of VML repair. Recently, PGS-based biomaterials have become an attractive material for tissue engineering applications in dynamic tissues due to its biocompatibility, biodegradability, elasticity, tunable mechanical properties, and degradation behavior [43,46]. PGS-based biomaterials have been applied to various tissue engineering applications such as liver [60], vasculature

[61], cardiac tissue [62–66], wound healing [67], and nerve [57]. This study demonstrated the first application of a DLP-based 3D printed PGSA for skeletal muscle tissue engineering. The results of this study demonstrate five key findings: 1) the ability to successfully 3D print elastic PGSA scaffold with hollow microchannel structures and 10-20 µm microgrooves, 2) the ability to modulate pure PGSA's mechanical properties through light intensity during 3D printing, 3) a novel transfection based approach to investigate cellular mechanisms inside of hollow, 3D PGSA scaffolds, 4) the development of an *in-vitro* VML model to study muscle progenitor cellular infiltration, proliferation, and maturation within an intact 3D printed PGSA scaffold for VML repair *in vivo*.

Many studies evaluating polymeric scaffolds in-vitro for VML treatment either rely on direct encapsulation of cells within the polymeric matrix, as in the cases of most hydrogels, or direct seeding onto the scaffold itself [9,10,12,14,17,19,20,26-28,30-35]. These methods, however, do not accurately mimic the application of an acellular scaffold for VML repair, which must recruit and facilitate migration of endogenous muscle progenitor cells before they can populate the scaffold through proliferation. A deliberate decision was made to study acellular scaffolds, as currently there are no clinical trials where xenogeneic or allogenic derived cellularized tissues are used for VML repair. In this study, we developed an in-vitro VML model to study alignment, proliferation, and differentiation response of iRFP-C2C12 cells as they migrate to and populate de novo within a 3D PGSA scaffold. To inform a more clinically motivated study, cells were seeded around the peripheral ends of the microchannel scaffold and allowed to migrate into the scaffold naturally over time to recapitulate the repair phase in VML treatment whereby residing muscle progenitor cells are recruited to infiltrate, proliferate, and differentiate within an implanted scaffold. To support future translational studies, we investigated the effect of channels size on cellular alignment, proliferation, and differentiation. The channel diameters were chosen to provide an environment where cells can fully populate the channel in vitro in 3D to form muscle bundles.

Previous groups have demonstrated the ability to modulate PGSA's mechanical properties through the variation in the degree of acrylation [68,69]. Previous work in our lab has demonstrated the ability to modulate the mechanical properties of PGSA through the duration of light exposure using a DLP-based printing system [70]. Here, we demonstrated a facile method to modulate PGSA's stiffness through the tuning of light intensity used for DLP-based 3D printing of PGSA with constant exposure time. By varying the light intensity, PGSA's stiffness can easily be tuned with an effective Young's modulus ranging from 134.5 kPa to 1.1 MPa. This occurs since the kinetic chain length of photopolymerizable polymer decreases as the light intensity used for photopolymerizable process increases [71]. Once the chain length of PGSA becomes shorter as a result of increased light intensity used for photopolymerization, the degree of crosslinking increases as a result, and thus the polymer chains are forced into a more restricted formation with resultant increase in stiffness [72]. Precision tuning mechanical properties using light has several advantages over synthesizing multiple formulations of PGSA with different degrees of acrylation, including the ability to quickly fabricate a single structure with heterogeneous material properties out of a bioink, which may more accurately replicate complex tissues such as the muscle-tendon interface. Since printing PGSA at the light intensity of 5.6 mW  ${\rm cm}^{-2}$  yielded an effective Young's modulus of 134.5 kPa, which is similar to the specific tension of skeletal muscle (107 kPa-225 kPa) [49-52], subsequent PGSA scaffolds used in this study were printed at this light intensity.

In order to engineer physiologically relevant tissues using acellular scaffolds, the ability to fabricate scaffolds with complex shapes in micron-scale resolution along with the ability to modulate the mechanical properties to match that of the tissue of interest is necessary [73-75]. The fabrication techniques currently used to create PGS-based scaffolds for tissue engineering applications [61,63,67,76-78] are limited to scaffolds of basic geometries due to the lack of fabrication techniques for high architectural complexity and fine features. By functionalizing PGS with acrylate groups to create PGSA, we demonstrated the ability to 3D print PGSA into an acellular PGSA scaffold with hollow anisotropically aligned microchannels of varying sizes (300-600  $\mu m)$  with longitudinal microgrooves (10-20  $\mu m)$  on the microchannel surface. The traditional approach to fabricate PGSA scaffolds requires harsh processing conditions (curing at high temperature and low pressure) that make it difficult to precision engineer structures with fine features and material properties [43]. By printing PGSA in a continuous fashion through our DLP-based 3D printing system, scaffolds possessing fine features with micron scale resolution were fabricated within a matter of minutes, a feat that cannot be readily achieved through

common traditional extrusion-based 3D printing systems [79]. The aligned microgroove features measuring  $10-20 \mu m$  in diameter that were observed within the inner channels of our 3D printed PGSA microchannel scaffolds are due to pixilation from the DMD chip under continuous printing process in our DLP-based 3D printing platform [80]. In a DLP-based 3D printing system, DMD chip consists of thousands of tiny square sized micromirrors that are used for optical pattern manipulation. Microgroove topographical features are an accompanying feature that were created from the pixel size or resolution of the DMD chip, due to the digitization of continuous objects into discrete pixelated masks [80]. Topotactic cues from microgroove pattern with similar widths have been previously demonstrated to influence alignment, proliferation, and myotube formation of C2C12 cells [81,82]. Thus, the presence of microgrooves within the microchannels of our PGSA scaffold may play a role in aiding the alignment, proliferation, and differentiation of skeletal muscle cells in VML treatment applications.

The evaluation of cellular response within a 3D PGSA construct through the use of either fluorescence or confocal imaging is extremely challenging due to its opacity and high autofluorescence in blue, which is a commonly reserved excitation/emission (359 nm/457 nm) spectrum used by DAPI staining to label cell nuclei [57]. To our knowledge, no attempts have been made to image cells through fluorescence or confocal imaging within an intact 3D PGSA construct, possibly due to noise from the material's autofluorescence. Longitudinal sectioning and imaging these constructs is not an option, as the sectioning process can disturb the natural organization of cells within the channel. To overcome this feature, initial attempts were made to stain the cell nuclei using a far-red nuclear dye (DRAQ5) outside of the scaffold's autofluorescence range. However, DRAQ5 was found to physically adsorb onto the PGSA scaffold within a few seconds of staining, resulting in noise from the scaffold upon confocal imaging, which did not allow for cells to be visualized within the 3D microchannel structure. As an alternative strategy to visualize the cells populating the 3D PGSA scaffold, an isogenic iRFP-C2C12 cell line was created through lentiviral transfection. By using iRFP-C2C12 cells to populate the scaffold de novo, clear visualization of cell nuclei within the 3D PGSA microchannel was achieved. Since previous studies have utilized iRFP for deep tissue imaging due to its emission of near-infrared light with long attenuation length [83-85], we hypothesized that transfecting C2C12 cells to express near-infrared fluorescent proteins in their nuclei would facilitate the imaging of cell nuclei within an intact 3D microchannel PGSA scaffold with high signal-to-noise ratio.

Microscale topographical cues have been revealed to play an important role in cellular migration, alignment, proliferation, and differentiation through mediated contact guidance interaction between the cells and biophysical cues from their microenvironment [86-89]. In addition to biophysical cues from the scaffold, biochemical cues are also important. In this study, dECM was employed as a coating to the PGSA scaffold to investigate its effect on cellular response of muscle cells since ECM sequesters growth factors, proteoglycans, and proteins thought to be involved in tissue regeneration [90,91]. Gastrocnemius muscle dECM was chosen as the dECM coating of choice, as it has been previously shown that skeletal muscle cells proliferate and differentiate better when cultured on a substrate coated with dECM that had the same tissue of origin as the cells [92]. In this study a single dECM concentration was evaluated, based on a previous study investigating dECM on improving blood perfusion in an animal model of ischemia [55]. However, the in vitro model of VML repair developed in this manuscript not only provides an excellent platform to study the effect of dose concentration of dECM on skeletal muscle infiltration, proliferation, and differentiation, but also is a platform to study other biologic applications such as sustained growth factor release. Furthermore, this platform can be developed to incorporate more cell types to more accurately model common obstacles for VML repair such as inflammation and fibrotic encapsulation of biomaterials after VML implantation.

A preliminary investigation was performed to assess the regenerative

capacity of a 3D printed PGSA scaffold for VML repair in vivo. Overall, cellular infiltration was observed deep into the scaffold, including the formation of new muscle fibers at 28 days. Interestingly, the general pattern of tissue infiltration that was observed - a fibrotic core with radial muscle formation – is characteristic of neonatal muscle formation [93]. While unexpected, this suggests two things: 1) the mechanisms governing skeletal muscle formation in an aligned scaffold is inherently different than that of normal muscle regeneration in a VML injury and 2) the 28-day timepoint is likely too early for muscle to resolve a VML injury in an acellular scaffold. The goal of this preliminary study was to determine if a PGSA scaffold can be used to regenerate aligned muscle tissue in vivo. In conjunction with the thorough in vitro investigation, these findings support that a 3D printed PGSA scaffold may provide an environment for skeletal muscle regeneration after VML injury. However more studies are required to better understand the complicated timeline and complex mechanisms of regeneration which are difficult to replicate in vitro.

There are a few limitations to the in vitro PGSA model that was demonstrated in this study. First, this model only recapitulates the regeneration and remodeling phase of muscle healing after a VML injury. For simplicity, the initial destruction phase with associated inflammatory response was not modeled to simplify this in vitro model. In practice, a VML injury is often associated with additional comorbidities that are often addressed prior to VML repair. During this initial phase, there is often scarring at the damaged tissue site. Prior to VML treatment, the newly formed scar tissue is removed via debridement, exposing healthy underlying tissue with which to integrate with the implanted autologous tissue or tissue engineered dECM sheet. Seeding muscle progenitor cells around the scaffold in vitro was chosen to replicate the phase of recovery at which VML injuries are often repaired. Second, this study did not utilize differentiation media to promote MHC expression. This was chosen to determine if the scaffold geometry and/ or dECM coating was sufficient to promote maturation of myoblasts in vitro. As a result, in the PGSA only scaffold, MHC+ fibers had a rounded, punctate phenotype, indicative of a nascent differentiation stage [94]. However, in the dECM coated scaffolds, a more elongated MHC+ phenotype was observed, suggesting while PGSA may provide an appropriate mechanical and microstructural environment for myotube maturation, extra biochemical modulation is required to have typical phenotypic expression of myotube maturation. Last, the in vivo preliminary studies were performed in parallel with the in vitro studies. Therefore, we chose a 450 µm channel size before the in vitro experiments yielded that a 600 µm channel size may provide enhanced mature MHC formation. Larger channel sizes will be evaluated in future in vivo studies.

# 5. Conclusions

This study demonstrated a novel application of a biocompatible elastomer (PGSA) as a 3D scaffold material for modeling the regeneration and remodeling phases of skeletal muscle after VML injury. By controlling the light intensity during DLP-based 3D printing, the material properties of PGSA were fine-tuned to be similar to the specific tension of skeletal muscle. To bypass issues associated with imaging cells within an autoflourescent 3D scaffold, an iRFP transfected C2C12 line was generated, allowing for visualization of cell nuclei within the scaffold. Once the scaffold parameters and imaging conditions were optimized, muscle progenitor cells were seeded around the outside of the scaffold, and cellular infiltration, proliferation, alignment, and maturation were assessed under different geometric (channel size) and biologic (dECM coating) cues. Overall, a dECM coated scaffold with 600  $\mu m$ diameter channels produced the best cellular infiltration, proliferation, alignment, and maturation of the experimental conditions evaluated. While this model was relatively simplified, this approach can be easily modified to investigate the use of alternative biomaterials (i.e. growth factors, CRISPR, dECM tissues/concentrations), cell types (i.e.

macrophages, fibroblasts, tenocyctes), and geometric cues (*i.e.* orientation, microstructure) on the recruitment and proliferation of muscle progenitor cells into acellular scaffolds.

# **Funding**

This work was supported in part by grants from the NIH to S.C. (R21AR074763), S.W. (R01AR070830-01), and N.H. (R01GM111458) and National Science Foundation (NSF) to S.C. (1903933, 2135720). W. K. is supported by the Anandamahidol Foundation.

#### CRediT authorship contribution statement

WK: Methodology, validation, investigation, formal analysis, resources, visualization, writing. DBB: conceptualization, methodology, formal analysis, investigation, writing, visualization, funding acquisition. AM: methodology. TF: methodology. AL: methodology. CY: methodology. Nan Hao: supervision. SRW: supervision, funding acquisition. SC: conceptualization, supervision, writing, funding acquisition. All authors contributed to the article and approved the submitted version.

# Declaration of competing interest

The authors have no conflicts of interest to declare.

#### Data availability

All data is available upon reasonable request to the corresponding authors.

# Acknowledgements

We thank Brendan Duggan from UCSD Skaggs School of Pharmacy and Pharmaceutical Sciences NMR Facility. We thank the University of California San Diego School of Medicine Microscopy Core for the imaging equipment and the technical support offered by Jennifer Santini and Marcella Erb. We thank Mary Esparza for her help with histology and animal care. The UCSD School of Medicine Microscopy Core facility was supported by National Institutes of Health (NIH) grant P30 NS047101. This work was supported in part by grants from the NIH to S. C. (R21AR074763), S.W. (R01AR070830-01), and N.H. (R01GM111458) and National Science Foundation (NSF) to S.C. (1903933). W.K. is supported by the Anandamahidol Foundation. The authors would like to thank Patricia Pizarro at the Center of Future of Surgery for providing the porcine muscle tissues used in this study.

# Appendix A. Supplementary data

Supplementary data to this article can be found online at https://doi. org/10.1016/j.bioadv.2022.213171.

# References

- R.L. Lieber, Skeletal Muscle Structure, Function, and Plasticity, Wolters Kluwer Health Adis (ESP), 2011.
- [2] Brian F. Grogan, J.R. Hsu, STRCVML. Volumetric muscle loss, Am Acad Orthop Surg. 19 (2011) S35–S37.
- [3] Anderson SE, Han WM, Srinivasa V, Mohiuddin M, Ruehle MA, Moon JY, et al. Determination of a Critical Size Threshold for Volumetric Muscle Loss in the Mouse Ouadriceps. doi:10.1089/ten.tec.2018.0324.
- [4] A. Eckardt, K. Fokas, Microsurgical reconstruction in the head and neck region: an 18-year experience with 500 consecutive cases, J. CranioMaxillofacial Surg. 31 (2003) 197–201.
- [5] B.D. Owens, J.F. Kragh, J.C. Wenke, J. Macaitis, C.E. Wade, J.B. Holcomb, Combat wounds in operation iraqi freedom and operation enduring freedom, J. Trauma Inj. Infect. Crit. Care 64 (2008) 295–299.

- [6] J.P. Mertens, K.B. Sugg, J.D. Lee, L.M. Larkin, Engineering muscle constructs for the creation of functional engineered musculoskeletal tissue, Regen. Med. 9 (2014) 89-100
- [7] M.M. Carleton, M. Locke, M.V. Sefton, Methacrylic acid-based hydrogels enhance skeletal muscle regeneration after volumetric muscle loss in mice, Biomaterials 275 (2021)
- [8] I.M. Basurto, M.T. Mora, G.M. Gardner, G.J. Christ, S.R. Caliari, Aligned and electrically conductive 3D collagen scaffolds for skeletal muscle tissue engineering, Biomater Sci. 9 (2021) 4040–4053.
- [9] Y. Jin, E.J. Jeon, S. Jeong, S. Min, Y.S. Choi, S.H. Kim, et al., Reconstruction of muscle fascicle-like tissues by anisotropic 3D patterning, Adv. Funct. Mater. 31 (2021) 1–19
- [10] B. Kasukonis, J. Kim, L. Brown, J. Jones, S. Ahmadi, T. Washington, et al., Codelivery of infusion decellularized skeletal muscle with minced muscle autografts improved recovery from volumetric muscle loss injury in a rat model, Tissue Eng. Part A. 22 (2016) 1151–1163.
- [11] Y. Zhang, Z. Zhang, Y. Wang, Y. Su, M. Chen, 3D myotube guidance on hierarchically organized anisotropic and conductive fibers for skeletal muscle tissue engineering, Mater Sci Eng C 116 (March) (2020) 111070.
- [12] E.L. Mintz, J.A. Passipieri, I.R. Franklin, V.M. Toscano, E.C. Afferton, P.R. Sharma, et al., Long-term evaluation of functional outcomes following rat volumetric muscle loss injury and repair, Tissue Eng. Part A 26 (2020) 140–156.
- [13] R.K. Bour, P.R. Sharma, J.S. Turner, W.E. Hess, E.L. Mintz, C.R. Latvis, et al., Bioprinting on sheet-based scaffolds applied to the creation of implantable tissueengineered constructs with potentially diverse clinical applications: tissueengineered muscle repair (TEMR) as a representative testbed, Connect. Tissue Res. 61 (2020) 216–228.
- [14] M. Costantini, S. Testa, E. Fornetti, C. Fuoco, C. Sanchez Riera, M. Nie, et al., Biofabricating murine and human myo-substitutes for rapid volumetric muscle loss restoration, EMBO Mol Med. 13 (2021) 1–17.
- [15] W.J. Kim, H. Lee, J.U. Lee, A. Atala, J.J. Yoo, S.J. Lee, et al., Efficient myotube formation in 3D bioprinted tissue construct by biochemical and topographical cues, Biomaterials 2020 (230) (July 2019), 119632.
- [16] Y. Jin, D. Shahriari, E.J. Jeon, S. Park, Y.S. Choi, J. Back, et al., Functional skeletal muscle regeneration with thermally drawn porous fibers and reprogrammed muscle progenitors for volumetric muscle injury, Adv. Mater. (2021), https://doi. org/10.1002/adma.202007946.
- [17] E.K. Merritt, D.W. Hammers, M. Tierney, L.J. Suggs, T.J. Walters, R.P. Farrar, Functional assessment of skeletal muscle regeneration utilizing homologous extracellular matrix as scaffolding, Tissue Eng - Part A. 16 (2010) 1395–1405.
- [18] J. Gilbert-Honick, S.R. Iyer, S.M. Somers, H. Takasuka, R.M. Lovering, K. R. Wagner, et al., Engineering 3D skeletal muscle primed for neuromuscular regeneration following volumetric muscle loss, Biomaterials 255 (2020), 120154.
- [19] Y.W. Cheng, D.J. Shiwarski, R.L. Ball, K.A. Whitehead, A.W. Feinberg, Engineering aligned skeletal muscle tissue using decellularized plant-derived scaffolds, ACS Biomater Sci Eng. 6 (2020) 3046–3054.
- [20] H.W. Kang, S.J. Lee, I.K. Ko, C. Kengla, J.J. Yoo, A. Atala, A 3D bioprinting system to produce human-scale tissue constructs with structural integrity, Nat. Biotechnol. 34 (2016) 312–319.
- [21] J.M. Grasman, D.M. Do, R.L. Page, G.D. Pins, Rapid release of growth factors regenerates force output in volumetric muscle loss injuries, Biomaterials 72 (2015) 49–60.
- [22] J. Zhang, Z.Q. Hu, N.J. Turner, S.F. Teng, W.Y. Cheng, H.Y. Zhou, et al., Perfusion-decellularized skeletal muscle as a three-dimensional scaffold with a vascular network template, Biomaterials 89 (2016) 114–126.
- [23] K.H. Nakayama, C. Alcazar, G. Yang, M. Quarta, P. Paine, L. Doan, et al., Rehabilitative exercise and spatially patterned nanofibrillar scaffolds enhance vascularization and innervation following volumetric muscle loss. Npj, Regen. Med. (2018); 3.
- [24] S. Das, K.D. Browne, F.A. Laimo, J.C. Maggiore, M.C. Hilman, H. Kaisaier, et al., Pre-innervated tissue-engineered muscle promotes a pro-regenerative microenvironment following volumetric muscle loss, Commun Biol. 3 (2020) 1–14.
- [25] J.P. Quint, A. Mostafavi, Y. Endo, A. Panayi, C.S. Russell, A. Nourmahnad, et al., In vivo printing of nanoenabled scaffolds for the treatment of skeletal muscle injuries, Adv Healthc Mater. (2021) 10.
- [26] J. Gilbert-Honick, S.R. Iyer, S.M. Somers, H. Takasuka, R.M. Lovering, K. R. Wagner, et al., Engineering 3D skeletal muscle primed for neuromuscular regeneration following volumetric muscle loss, Biomaterials 255 (2020), 120154.
- [27] W.J. Kim, H. Lee, J.U. Lee, A. Atala, J.J. Yoo, S.J. Lee, et al., Efficient myotube formation in 3D bioprinted tissue construct by biochemical and topographical cues, Biomaterials 2020 (230) (July 2019), 119632.
- [28] Y. Zhang, Z. Zhang, Y. Wang, Y. Su, M. Chen, 3D myotube guidance on hierarchically organized anisotropic and conductive fibers for skeletal muscle tissue engineering, Mater Sci Eng C. (2020) 116. March:111070.
- [29] B. Basturkmen, E. Ergene, D. Doganay, P. Yilgor Huri, H.E. Unalan, E.A. Aksoy, Silver nanowire loaded poly(e-caprolactone) nanocomposite fibers as electroactive scaffolds for skeletal muscle regeneration, Mater. Sci. Eng. C Mater. Biol. Appl. 134 (2021), 112567.
- [30] R.K. Bour, P.R. Sharma, J.S. Turner, W.E. Hess, E.L. Mintz, C.R. Latvis, et al., Bioprinting on sheet-based scaffolds applied to the creation of implantable tissueengineered constructs with potentially diverse clinical applications: tissueengineered muscle repair (TEMR) as a representative testbed, Connect. Tissue Res. 61 (2020) 216–228.
- [31] I.M. Basurto, M.T. Mora, G.M. Gardner, G.J. Christ, S.R. Caliari, Aligned and electrically conductive 3D collagen scaffolds for skeletal muscle tissue engineering, Biomater Sci. 9 (2021) 4040–4053.

- [32] J.M. Grasman, D.M. Do, R.L. Page, G.D. Pins, Rapid release of growth factors regenerates force output in volumetric muscle loss injuries, Biomaterials 72 (2015) 49–60.
- [33] J. Zhang, Z.Q. Hu, N.J. Turner, S.F. Teng, W.Y. Cheng, H.Y. Zhou, et al., Perfusion-decellularized skeletal muscle as a three-dimensional scaffold with a vascular network template, Biomaterials 89 (2016) 114–126.
- [34] K.H. Nakayama, C. Alcazar, G. Yang, M. Quarta, P. Paine, L. Doan, et al., Rehabilitative exercise and spatially patterned nanofibrillar scaffolds enhance vascularization and innervation following volumetric muscle loss. Npj, Regen. Med. (2018;) 3.
- [35] S. Das, K.D. Browne, F.A. Laimo, J.C. Maggiore, M.C. Hilman, H. Kaisaier, et al., Pre-innervated tissue-engineered muscle promotes a pro-regenerative microenvironment following volumetric muscle loss, Commun Biol. 3 (2020) 1–14.
- [36] A. Golchin, T.Z. Farahany, Biological products: cellular therapy and FDA approved products, Stem cell Rev reports. 15 (2019) 166–175.
- [37] J. Dziki, S. Badylak, M. Yabroudi, B. Sicari, F. Ambrosio, K. Stearns, et al., An acellular biologic scaffold treatment for volumetric muscle loss: results of a 13patient cohort study, NpjRegen. Med. (2016) 1.
- [38] B.M. Sicari, C.L. Dearth, S.F. Badylak, Tissue engineering and regenerative medicine approaches to enhance the functional response to skeletal muscle injury, Anat. Rec. 297 (2014) 51–64.
- [39] L.A. Loureiro dos Santos, Natural polymeric biomaterials: processing and properties ★, in: Reference Module in Materials Science and Materials Engineering, Elsevier, 2017.
- [40] V.T. Duong, T.T. Dang, C.H. Hwang, S.H. Back, K. Koo, Coaxial printing of double-layered and free-standing blood vessel analogues without ultraviolet illumination for high-volume vascularised tissue, Biofabrication 12 (2020), 045033.
- [41] M.C. Catoira, L. Fusaro, D. Di Francesco, M. Ramella, F. Boccafoschi, Overview of natural hydrogels for regenerative medicine applications, J Mater Sci Mater Med. 30 (2019).
- [42] M.S.B. Reddy, D. Ponnamma, R. Choudhary, K.K. Sadasivuni, A comparative review of natural and synthetic biopolymer composite scaffolds, Polymers (Basel) (2021) 13.
- [43] Y. Wang, G.A. Ameer, B.J. Sheppard, R. Langer, A tough biodegradable elastomer, Nat. Biotechnol. 20 (2002) 602–606.
- [44] C.C. Lau, M. Al Qaysi, N. Owji, M.K. Bayazit, J. Xie, J.C. Knowles, et al., Advanced biocomposites of poly(glycerol sebacate) and β-tricalcium phosphate by in situ microwave synthesis for bioapplication, Mater Today Adv. 5 (2020), 100023.
- [45] P. Wang, D.B. Berry, Z. Song, W. Kiratitanaporn, J. Schimelman, A. Moran, et al., 3D printing of a biocompatible double network elastomer with digital control of mechanical properties, Adv. Funct. Mater. 30 (2020) 1–9.
- [46] C.L.E. Nijst, J.P. Bruggeman, J.M. Karp, L. Ferreira, A. Zumbuehl, C.J. Bettinger, et al., Synthesis and characterization of photocurable elastomers from poly(glycerolco-sebacate), Biomacromolecules 8 (2007) 3067–3073.
- [47] A.P. Zhang, X. Qu, P. Soman, K.C. Hribar, J.W. Lee, S. Chen, et al., Rapid fabrication of complex 3D extracellular microenvironments by dynamic optical projection stereolithography, Adv. Mater. 24 (2012) 4266–4270.
- [48] J.R. Tumbleston, D. Shirvanyants, N. Ermoshkin, R. Janusziewicz, A.R. Johnson, D. Kelly, et al., Continuous liquid interface production of 3D objects, Science (80-) 347 (2015) 1349–1352.
- [49] R.L. Lieber, M.E. Leonard, C.G. Brown, C.L. Trestik, Frog semitendinosis tendon load-strain and stress-strain properties during passive loading, Am. J. Phys. 261 (1 Pt 1) (1991) C86–C92.
- [50] C.N. Maganaris, V. Baltzopoulos, D. Ball, A.J. Sargeant, In vivo specific tension of human skeletal muscle, J. Appl. Physiol. 90 (2001) 865–872.
- [51] P.L. Powell, R.R. Roy, P. Kanim, M.A. Bello, V.R. Edgerton, Predictability of skeletal muscle tension from architectural determinations in Guinea pig hindlimbs, J. Appl. Physiol. Respir. Environ. Exerc. Physiol. 57 (1984) 1715–1721.
- [52] R.I. Close, Dynamic properties of mammalian skeletal muscles, Physiol. Rev. 52 (1972) 129–197.
- [53] R.L. Lieber, S.R. Ward, Skeletal muscle design to meet functional demands, Philos. Trans. R. Soc. B Biol. Sci. 366 (2011) 1466–1476.
- [54] W. Zhu, X. Qu, J. Zhu, X. Ma, S. Patel, J. Liu, et al., Direct 3D bioprinting of prevascularized tissue constructs with complex microarchitecture, Biomaterials 124 (2017) 106–115.
- [55] M.J. Hernandez, E.I. Zelus, M.T. Spang, R.L. Braden, K.L. Christman, Dose optimization of decellularized skeletal muscle extracellular matrix hydrogels for improving perfusion and subsequent validation in an aged hindlimb ischemia model, Biomater Sci. 8 (2020) 3511–3521.
- [56] S.V. Kontomaris, A. Malamou, Hertz model or Oliver & Pharr analysis? Tutorial regarding AFM nanoindentation experiments on biological samples, Mater. Res. Express. (2020) 7.
- [57] D. Singh, A.J. Harding, E. Albadawi, F.M. Boissonade, J.W. Haycock, F. Claeyssens, Additive manufactured biodegradable poly(glycerol sebacate methacrylate) nerve guidance conduits, Acta Biomater. 78 (2018) 48–63.
- [58] A. Marsano, R. Maidhof, L.Q. Wan, Y. Wang, J. Gao, N. Tandon, et al., Scaffold stiffness affects the contractile function of three-dimensional engineered cardiac constructs, Biotechnol. Prog. 26 (2010) 1382–1390.
- [59] M. Ogrodnik, H. Salmonowicz, R. Brown, J. Turkowska, W. Sredniawa, S. Pattabiraman, et al., Dynamic JUNQ inclusion bodies are asymmetrically inherited in mammalian cell lines through the asymmetric partitioning of vimentin, Proc. Natl. Acad. Sci. U. S. A. 111 (2014) 8049–8054.
- [60] C.L. Teng, J.Y. Chen, T.L. Chang, S.K. Hsiao, Y.K. Hsieh, K.A. Villalobos Gorday, et al., Design of photocurable, biodegradable scaffolds for liver lobule regeneration via digital light process-additive manufacturing, Biofabrication 12 (2020).

- [61] D. Motlagh, J. Yang, K.Y. Lui, A.R. Webb, G.A. Ameer, Hemocompatibility evaluation of poly(glycerol-sebacate) in vitro for vascular tissue engineering, Biomaterials 27 (2006) 4315–4324.
- [62] Q.-Z. Chen, A. Bismarck, U. Hansen, S. Junaid, M.Q. Tran, S.E. Harding, et al., Characterisation of a soft elastomer poly(glycerol sebacate) designed to match the mechanical properties of myocardial tissue, Biomaterials 29 (2008) 47–57.
- [63] M.J.N. Pereira, B. Ouyang, C.A. Sundback, N. Lang, I. Friehs, S. Mureli, et al., A highly tunable biocompatible and multifunctional biodegradable elastomer, Adv. Mater. 25 (2013) 1209–1215.
- [64] R. Rai, M. Tallawi, N. Barbani, C. Frati, D. Madeddu, S. Cavalli, et al., Biomimetic poly(glycerol sebacate) (PGS) membranes for cardiac patch application, Mater Sci Eng C. 33 (2013) 3677–3687.
- [65] Q.-Z. Chen, H. Ishii, G.A. Thouas, A.R. Lyon, J.S. Wright, J.J. Blaker, et al., An elastomeric patch derived from poly(glycerol sebacate) for delivery of embryonic stem cells to the heart, Biomaterials 31 (2010) 3885–3893.
- [66] M.D. Guillemette, H. Park, J.C. Hsiao, S.R. Jain, B.L. Larson, R. Langer, et al., Combined Technologies for Microfabricating Elastomeric Cardiac Tissue Engineering Scaffolds, Macromol. Biosci. 10 (2010) 1330–1337.
- [67] A. Tamayol, A. Hassani Najafabadi, P. Mostafalu, A.K. Yetisen, M. Commotto, M. Aldhahri, et al., Biodegradable elastic nanofibrous platforms with integrated flexible heaters for on-demand drug delivery, Sci. Rep. 7 (2017) 1–10.
- [68] C.L.E. Nijst, J.P. Bruggeman, J.M. Karp, L. Ferreira, A. Zumbuehl, C.J. Bettinger, et al., Synthesis and characterization of photocurable elastomers from poly(glycerolco-sebacate), Biomacromolecules 8 (2007) 3067–3073.
- [69] Y.L. Wu, A.R. D'Amato, A.M. Yan, R.Q. Wang, X. Ding, Y. Wang, Three-dimensional printing of Poly(glycerol sebacate) acrylate scaffolds via digital light processing, ACS Appl. Bio Mater. 3 (2020) 7575–7588.
- [70] P. Wang, X. Li, W. Zhu, Z. Zhong, A. Moran, W. Wang, et al., 3D bioprinting of hydrogels for retina cell culturing, Bioprinting (2018) 1–6.
- [71] C. Decker, Kinetic study and new applications of UV radiation curing, Macromol. Rapid Commun. 23 (2002) 1067–1093.
- [72] S.H. Pyo, P. Wang, H.H. Hwang, W. Zhu, J. Warner, S. Chen, Continuous optical 3D printing of green aliphatic polyurethanes, ACS Appl. Mater. Interfaces 9 (2017) 836–844
- [73] A.J. Engler, S. Sen, H.L. Sweeney, D.E. Discher, Matrix elasticity directs stem cell lineage specification, Cell 126 (2006) 677–689.
- [74] D. Li, J. Zhou, F. Chowdhury, J. Cheng, N. Wang, F. Wang, Role of mechanical factors in fate decisions of stem cells, Regen. Med. 6 (2011) 229–240.
- [75] L. Ghasemi-Mobarakeh, Structural properties of scaffolds: crucial parameters towards stem cells differentiation, World J. Stem Cells. 7 (2015) 728.
- [76] Q.-Z. Chen, H. Ishii, G.A. Thouas, A.R. Lyon, J.S. Wright, J.J. Blaker, et al., An elastomeric patch derived from poly(glycerol sebacate) for delivery of embryonic stem cells to the heart, Biomaterials 31 (2010) 3885–3893.
- [77] Q.-Z. Chen, A. Bismarck, U. Hansen, S. Junaid, M.Q. Tran, S.E. Harding, et al., Characterisation of a soft elastomer poly(glycerol sebacate) designed to match the mechanical properties of myocardial tissue. Biomaterials 29 (2008) 47–57.

- [78] R. Rai, M. Tallawi, N. Barbani, C. Frati, D. Madeddu, S. Cavalli, et al., Biomimetic poly(glycerol sebacate) (PGS) membranes for cardiac patch application, Mater Sci Eng C. 33 (2013) 3677–3687.
- [79] A. Panwar, L.P. Tan, Current status of bioinks for micro-extrusion-based 3D bioprinting, Molecules 21 (2016).
- [80] C.J. Pateman, A.J. Harding, A. Glen, C.S. Taylor, C.R. Christmas, P.P. Robinson, et al., Nerve guides manufactured from photocurable polymers to aid peripheral nerve repair, Biomaterials 49 (2015) 77–89.
- [81] H. Gao, J. Xiao, Y. Wei, H. Wang, H. Wan, S. Liu, Regulation of myogenic differentiation by topologically microgrooved surfaces for skeletal muscle tissue engineering, ACS Omega 6 (2021) 20931–20940.
- [82] L. Altomare, N. Gadegaard, L. Visai, M.C. Tanzi, S. Farè, Biodegradable microgrooved polymeric surfaces obtained by photolithography for skeletal muscle cell orientation and myotube development, Acta Biomater. 6 (2010) 1948–1957.
- [83] G.S. Filonov, K.D. Piatkevich, L.M. Ting, J. Zhang, K. Kim, V.V. Verkhusha, Bright and stable near-infrared fluorescent protein for in vivo imaging, Nat. Biotechnol. 29 (2011) 757–761.
- [84] X. Zhang, S. Bloch, W. Akers, S. Achilefu, Near-infrared molecular probes for in vivo imaging, Curr Protoc Cytom. (2012), https://doi.org/10.1002/0471142956. cv1227560
- [85] C. Hall, Y. von Grabowiecki, S.P. Pearce, C. Dive, S. Bagley, P.A.J. Muller, iRFP (near-infrared fluorescent protein) imaging of subcutaneous and deep tissue tumours in mice highlights differences between imaging platforms, Cancer Cell Int. 21 (2021) 1–15.
- [86] P. Rørth, Whence directionality: guidance mechanisms in solitary and collective cell migration, Dev. Cell 20 (2011) 9–18.
- [87] C.S. Chen, M. Mrksich, S. Huang, G.M. Whitesides, D.E. Ingber, Geometric control of cell life and death, Science (80-) 276 (1997) 1425–1428.
- [88] M. Nikkhah, F. Edalat, S. Manoucheri, A. Khademhosseini, Engineering microscale topographies to control the cell-substrate interface, Biomaterials 33 (2012) 5230–5246.
- [89] L. Altomare, N. Gadegaard, L. Visai, M.C. Tanzi, S. Farè, Biodegradable microgrooved polymeric surfaces obtained by photolithography for skeletal muscle cell orientation and myotube development, Acta Biomater. 6 (2010) 1948–1957.
- [90] K. Garg, C.L. Ward, C.R. Rathbone, B.T. Corona, Transplantation of devitalized muscle scaffolds is insufficient for appreciable de novo muscle fiber regeneration after volumetric muscle loss injury, Cell Tissue Res. 358 (2014) 857–873.
- [91] C. Frantz, K.M. Stewart, V.M. Weaver, The extracellular matrix at a glance, J. Cell Sci. 123 (2010) 4195–4200.
- [92] Y. Zhang, Y. He, S. Bharadwaj, N. Hammam, K. Carnagey, R. Myers, et al., Tissue-specific extracellular matrix coatings for the promotion of cell proliferation and maintenance of cell phenotype, Biomaterials 30 (2009) 4021–4028.
- [93] D.S. Gokhin, S.R. Ward, S.N. Bremner, R.L. Lieber, Quantitative analysis of neonatal skeletal muscle functional improvement in the mouse, J. Exp. Biol. 211 (2008) 837–843.
- [94] B.R. Seo, C.J. Payne, S.L. McNamara, B.R. Freedman, B.J. Kwee, S. Nam, et al., Skeletal muscle regeneration with robotic actuation-mediated clearance of neutrophils, Sci. Transl. Med. (2021) 13.